Wind-Driven Mechanisms for the Variations of the Pacific Equatorial Undercurrent Based on Adjoint Sensitivity Analysis

Jin Wang [1,2], Chuanyu Liu [1,3,4*], Xiaowei Wang [1,3,4], Armin Köhl [5], Yilong Lyu [1,3], Yuanlong Li [1,3,4] and Fan Wang [1,2,3,4]

[1] Key Laboratory of Ocean Circulation and Waves, Institute of Oceanology, Chinese Academy of Sciences, Qingdao, China, [2] University of Chinese Academy of Sciences, Beijing, China, [3] Center for Ocean Mega-Science, Chinese Academy of Sciences, Qingdao, China, [4] Marine Dynamic Process and Climate Function Laboratory, Pilot National Laboratory for Marine Science and Technology (Qingdao) (QNLM), Qingdao, China, [5] Institute of Oceanography (ifm), Center for Earth System Research and Sustainability (CEN), University of Hamburg, Hamburg, Germany

The maintenance and variation of the Pacific Equatorial Undercurrent (EUC) are thought to be controlled by the zonal pressure gradient force (ZPGF). However, a recent study found that a large-scale circulation associated with Rossby waves can also lead to EUC variation, implying that the structures and timing of the influential winds and the underlying wind-driven mechanisms need to be revisited. Here, we use the adjoint-sensitivity method to obtain the crucial winds that can most efficiently influence EUC variations. The obtained adjoint sensitivities (denoting the sensitive winds) are confined to 15°S–15°N and exhibit a funnel-shaped pattern with high symmetry about the equator. The remote winds, which occur 4 to 11 months prior, can lead to EUC variations at the basin scale; in contrast, the near-term winds (occurring not earlier than 4 months) lead only to local EUC variations. Accordingly, we find that wind-initiated equatorial Kelvin waves, equatorial Rossby waves, and the reflected waves at both the western and eastern boundaries superimpose onto each other to result in EUC variations. Specifically, when the travel time is longer than 4 months, the waves can form a negative-positive-negative sea surface height anomaly (SSHA) pattern between 15°S and 15°N in the central-eastern tropical Pacific, indicating the joint effect of both types of waves; they also form a positive SSHA in the western equatorial Pacific, indicating the dominance of the Kelvin wave therein. These mechanisms are complementary to the canonical ZPGF mechanism, which provide a clear theoretical basis for EUC variation studies.

Keywords: Equatorial Undercurrent, adjoint sensitivity analysis, equatorial Rossby wave, Kelvin wave, wind-driven

1 INTRODUCTION

The Equatorial Undercurrent (EUC) in the Pacific Ocean (Cromwell et al., 1954) flows eastward along the equator with a thickness of ~200 m and a width of about 400 km. It is generally centered at 50 to 200 m depth and slopes upward to the east along the equatorial thermocline (Kessler et al., 1998), with a zonal mass transport of 30–40 Sv (1 Sv=1 ×10^6 m^3 s^{-1}; Johnson et al., 2002; Izumo, 2005; Halpern

et al., 2015). As the strongest subsurface current in the equatorial current system, the EUC transports warm, high-salinity, nutrient-rich, and CO_2-rich water eastward, maintaining the zonal balance of water mass and heat in the equatorial Pacific Ocean (e.g., McCreary, 1976; Pennington et al., 2006; Qin et al., 2015; Coats and Karnauskas, 2018). The EUC can also modulate the El Niño and Southern Oscillation (ENSO) by its variations in heat/mass transport (e.g., Johnson et al., 2000; Izumo, 2005; Lyu et al., 2020). Therefore, depicting the strength of the EUC and understanding its variability are of great significance to exploring the dynamics and climate impacts of the equatorial current system (Hu et al., 2015).

The trade winds in the tropical Pacific have always been deemed the leading predictor of the EUC in previous studies. For example, Pedlosky (1987) argued that the relation of EUC transport (EUCT) to wind stress (τ) should be $EUCT \sim \tau^{7/8}$ under inertial nonlinear theory, which is similar to the quasi-linear relationship by Yu and Mcphaden (1999). Liu and Philander (1995) demonstrated that the EUC tends to fade when the tropical easterly wind disappears in a model simulation. Using a reconstruction of EUC strength with the TAO array, Izumo (2005) shows that weakened equatorial trade winds in the western and central Pacific can reduce the EUC strength to the east of the trade wind after 3 months. Drenkard and Karnauskas (2014) also revealed a regime in the eastern Pacific where weakened trade winds reduced EUC strength.

The EUC is primarily driven by the accumulated water in the west Pacific, which drives the subsurface eastward pressure gradient force (EPGF). Therefore, the wind-driven EPGF has long been considered as the canonical mechanism for EUC variation (Stommel, 1959; Pedlosky, 1987). Using current measurement data, Firing et al. (1983) verified that the disappearance of EUC during the summer of 1982 was due to the local weakening or reversal of the EPGF caused by the basin-wide adjustment of the sea surface slope to the strong westerly wind anomalies in the western and central Pacific, similar to the observations by Johnson et al. (2000). Yu and Mcphaden (1999), using TAO array data, argued that the momentum balance of the EUC is primarily between the EPGF and the zonal wind induced stresses, and that the zonal wind dominantly contributes to the EUC variations. However, studies usually focused on specific meridional sections of the EUC. Possibly due to the lack of coherent observations of EUC in the entire Equatorial Pacific, the wind patterns that cause basin-wide variations of the EUC and the underlying mechanism were not well explored. Reviewed from this aspect, previous studies usually overgeneralized the spatial pattern, timing, and locations of the effective zonal wind.

Recently, Lyu et al. (2020) proposed a different mechanism for the interannual variation of the EUC. Based on the Scientific Observing Network of the Chinese Academy of Sciences (CASSON), the authors found that the EUC was significantly enhanced at three mooring sites (142°E, 1°S), (142°E, 0°) and (140°E, 2°N) in the summer of 2016 relative to that in 2015. Using a 1.5-layer reduced-gravity ocean model, they found that the EUC at those mooring sites is strengthened by the southern part of a counterclockwise circulation straddling the equator.

Furthermore, it is revealed that the counterclockwise circulation is associated with Rossby waves generated by the reflection of equatorial Kelvin waves, which are triggered by easterly wind perturbations between 5°S and 5°N in the central-eastern Pacific basin approximately half a year prior to the EUC enhancement. Lyu et al. (2020)'s mechanism for the EUC variation can be considered as Rossby wave-associated "circulation" mechanism, which can be regarded as a complement to the canonical west-east pressure gradient mechanism. However, the anomalous circulation in their study is obviously regional, since their EUC sites are confined to the western boundary.

Nonetheless, Lyu et al. (2020) provided an interesting and important perspective on the mechanisms of EUC variation, which, however, also raises some questions:

1) Is their mechanism specific for EUCT variation near the western boundary? Is it applicable to other longitudes, times, and conditions?

2) For the EUCT in other certain sections, what pattern, from what locations, and how soon, will the wind most efficiently influence the EUC?

3) Are the expected winds able to cause EUC variation only locally, or can they lead to EUC variation in the basin scale? What are the underlying mechanisms?

Therefore, to better understand EUC variability, it is critical to depict in detail its sensitivity to wind at various temporal and spatial scales.

In this study, the adjoint model is employed to study the sensitivity of the EUCT to wind stresses in different regions and with different leading times. The adjoint model is the reversed propagator of the tangent linear model, which is a differential version of the original nonlinear model (Errico, 1997; Verdy et al., 2014). In sensitivity analysis, the adjoint model gets some unique advantages compared with the forward perturbation experiment (seen in **Figure S1**). The adjoint model can calculate the partial derivatives of all state variables relative to a targeted function around a time-dependent "forward" model trajectory, which can provide the sensitivities of each concerned variable at all grids (including both spatial and time grids) under the quasi-linear assumption. In contrast, a traditional forward perturbation experiment by the nonlinear model can only indicate the system responses to one predetermined perturbation in a specific location and leading time. Therefore, the adjoint model has been widely applied in understanding the dynamic mechanisms of sensitivity problems (e.g., Marotzke et al., 1999; Zhang et al., 2011; Verdy et al., 2014; Jones et al., 2018). Since the derived sensitivity to state variables usually determine the most effective descent direction [i.e., the optimal perturbation by Köhl and Vlasenko (2019)] in minimizing a misfit function, the adjoint model can also be used in the state estimation by 3D/4D Var data assimilation (e.g., Mazloff et al., 2010; Wang et al., 2021) and state prediction (Köhl and Vlasenko, 2019). For example, Mazloff et al. (2010) derived an Eddy-Permitting Southern Ocean State Estimate by MITgcm and its adjoint model. Köhl and Vlasenko (2019) used the obtained adjoint sensitivities to construct a theoretical prediction model for atmospheric temperature. In addition, the adjoint of the

tracer equations can also reveal the origins of the passive tracers and thus the circulation (Fukumori et al., 2004).

In the present study, we adopt the adjoint model from the German contribution to the Estimation of the Circulation and Climate of the Ocean (GECCO) system; as a result, the specific locations and structures of the winds affecting the EUCT variations (denoted the sensitive winds) are determined objectively. Consequently, the underlying mechanisms of wind-driven EUCT variations are identified, which provides new insights into the remote and local wind effects on EUCT variations.

The rest of the paper is organized as follows. In Section 2, we introduce the model configuration and the adjoint framework. A detailed analysis of the adjoint sensitivity is given in Section 3, including the distribution of the adjoint sensitivity, the influence of the sensitivity-like wind forcing perturbation on the EUCT, and the dynamic mechanisms. Finally, a summary and discussion are presented in Section 4.

2 MODEL AND METHODOLOGY

2.1 Model Configuration

The model used in this study comprises the Massachusetts Institute of Technology ocean circulation model (MITgcm; Marshall et al., 1997a) and its adjoint component (Marotzke et al., 1999), which are assembled in the 4D-Var (adjoint) synthesis of GECCO (Köhl and Stammer, 2008). GECCO is configured on 1°×1° horizontal grids and 23 unevenly spaced vertical levels, with vertical intervals ranging from 10–100 m in the upper layers and 200–500 m in the deep layers. The model covers a quasi-global ocean over ±80° latitude with realistic bottom topography based on the Earth Topography 5-arc-min grid (ETOPO5) dataset (Smith and Sandwell, 1997). Vertical mixing is represented by the K-Profile Parameterization (KPP) scheme (Large et al., 1994), with the background diffusivities and viscosities of 10^{-5} m^2 s^{-1} and 10^{-3} m^2 s^{-1}, respectively (Köhl et al., 2007). Gent-McWilliams (GM) and Redi's eddy parameterization schemes (Redi, 1982; Gent and Mcwilliams, 1990) are implemented, with both diffusivities being 800 m^2 s^{-1}.

The model is integrated forward for 30 years with a 3600-second time step, initiated with climatological temperature and salinity from the World Ocean Atlas 2013 (WOA13; Locarnini et al., 2013; Zweng et al., 2013) and forced by long-term climatology of 6-hourly surface heat flux, wind stress, and freshwater flux fields, which are obtained from the National Centers for Environmental Prediction (NCEP; Kalnay et al., 1996). As such, we produce a climatological ocean with only annual cycles. The integration of the first 20 years is the spin-up stage, while the outputs in the last 10 years are used to validate the seasonal variability of the EUCT, and those in the last 2 years are used for the adjoint-sensitivity calculation.

2.2 Adjoint Sensitivity Framework

An adjoint model calculates backward time-evolution of the linear sensitivity of the target function to the prognostic and input variables of the original model. The theoretical framework of adjoint sensitivity has been explained in detail by previous overviews (e.g., Errico, 1997; Junge and Haine, 2001). A brief description is given below for readers who may not be familiar with the adjoint method.

As for an ocean general circulation model, the model equations can be denoted simplistically as:

$$\mathbf{y} = \mathbf{M}_t(\mathbf{x}_0), t \in [0, T] \qquad (1)$$

where $\mathbf{M}_t$ refers to the nonlinear forward operator working on the state vector $\mathbf{x}$ at initial time $t = 0$, and $\mathbf{y} = \mathbf{x}_T$ means the state vector at final time T.

For a small perturbation $\delta\mathbf{x}_0$ at the initial time, its evolution at the final time T in the nonlinear system can be written as:

$$\delta\mathbf{y} = \mathbf{M}_t(\mathbf{x}_0 + \delta\mathbf{x}_0) - \mathbf{M}_t(\mathbf{x}_0) = \mathbf{L}_t\delta\mathbf{x}_0 \qquad (2)$$

where $\mathbf{L}_t = \partial\mathbf{M}_t/\partial\mathbf{x}_0$ represents the linearized dynamical operator. Equation (2) is a Taylor series expansion for the first order and is a linear model whose coefficients are determined by slopes tangent to the trajectories of the state variables in the forward model. Thus, it is also called a tangent linear model, which describes the linearized evolution of a state perturbation.

To obtain the adjoint sensitivity, a scale function J (i.e., the cost function) about the state variable $\mathbf{y}$ is defined according to the study interest, i.e., $J = J(\mathbf{y})$. For the small perturbation $\delta\mathbf{x}_0$, the difference of the cost function δJ can be expressed as the inner product of the sensitivity and the state perturbation under the tangent linear assumption, i.e.

$$\delta J = \langle \frac{\partial J}{\partial \mathbf{y}}, \delta\mathbf{y} \rangle = \langle \frac{\partial J}{\partial \mathbf{x}_0}, \delta\mathbf{x}_0 \rangle \qquad (3)$$

By the tangent linear operator $\mathbf{L}_t$ in Equation (2), Equation (3) changes to

$$\delta J = \langle \frac{\partial J}{\partial \mathbf{y}}, \delta\mathbf{y} \rangle = \langle \frac{\partial J}{\partial \mathbf{y}}, \mathbf{L}_t\delta\mathbf{x}_0 \rangle = \langle \mathbf{L}_t^\star \frac{\partial J}{\partial \mathbf{y}}, \delta\mathbf{x}_0 \rangle \qquad (4)$$

where $\mathbf{L}_t^\star$ is the corresponding adjoint operator of $\mathbf{L}_t$. Equivalently, by the equations (3) and (4), the adjoint sensitivity of the cost function of state variables can be obtained as:

$$\frac{\partial J}{\partial \mathbf{x}_0} = \mathbf{L}_t^\star \frac{\partial J}{\partial \mathbf{y}} \qquad (5)$$

Notably, Equation (5) has a crucial advantage over Equation (2). Because to obtain the sensitivities when using Equation (2), we have to run the tangent linear model by perturbing each $\delta\mathbf{x}_0$ element one by one over the concerned region; in contrast, using Equation (5), the adjoint model $\mathbf{L}_t^\star$ is applied to $\frac{\partial J}{\partial \mathbf{y}}$ at one integration, and as such, every time-stepping backward will yield the required sensitivity to all $\mathbf{x}_0$ elements. The schematic diagram of the relationship between the adjoint model and nonlinear model is shown in **Figure S2**. In practice, the target function can be feasibly defined, such as the area-mean sea surface temperature (Zhang et al., 2011), Atlantic heat transport (Marotzke et al., 1999), forecast errors in synoptic studies

(Errico, 1997), and model-observation deviations in particular used in 4D-Var data assimilation and parameter estimation (Köhl & Stammer, 2008; Liu et al., 2012; Köhl & Vlasenko, 2019).

In this work, the adjoint model of GECCO synthesis is generated *via* automatic/algorithmic differentiation with the Transformation of Algorithms in FORTRAN (TAF; Giering and Kaminski, 1998; Heimbach et al., 2005). The last two years of the climatological forward run with well-simulated annual

cycles of the EUCT are chosen as the "neutral" background for the adjoint calculation. Due to the high seasonality of the EUCT (as seen in **Figures 1**, **2**, the EUCT usually peaks in July), the target function *J* is defined as the monthly mean EUCT at 165°E in July of the second year:

$$J = \iint u \, dy \, dz, y \in [3\,°\mathrm{S}, 3\,°\mathrm{N}], z \in [87.5m, 310m], \qquad (6)$$
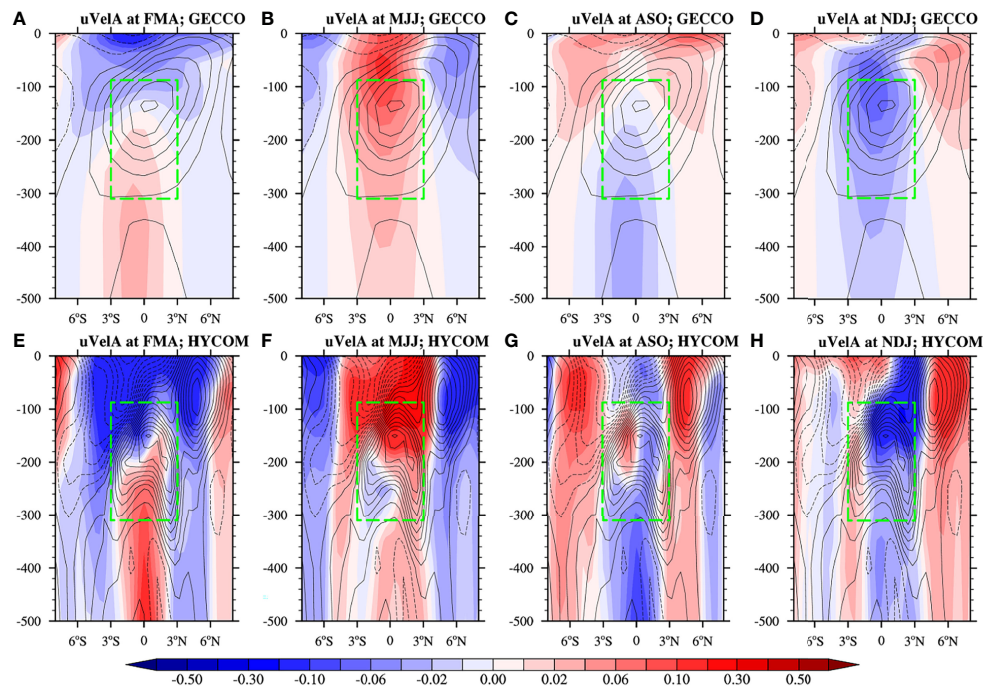

FIGURE 1 | Vertical structures of the climatological mean (contours; m s^{-1}) and seasonal anomalies (color shading; m s^{-1}) of the zonal velocity at 165°E derived from GECCO in boreal **(A)** spring, **(B)** summer, **(C)** autumn, **(D)** winter. **(E–H)** same as **(A–D)**, but from HYCOM. The solid lines represent the eastward velocity, and the dashed lines represent the westward velocity. The green dashed box represents the target section in the EUCT's calculation. The interval of the contours is 0.03 m s^{-1}. Note the nonlinear shading levels in the color bar, and the climatological zonal velocity of HYCOM is averaged between 1994 and 2013.
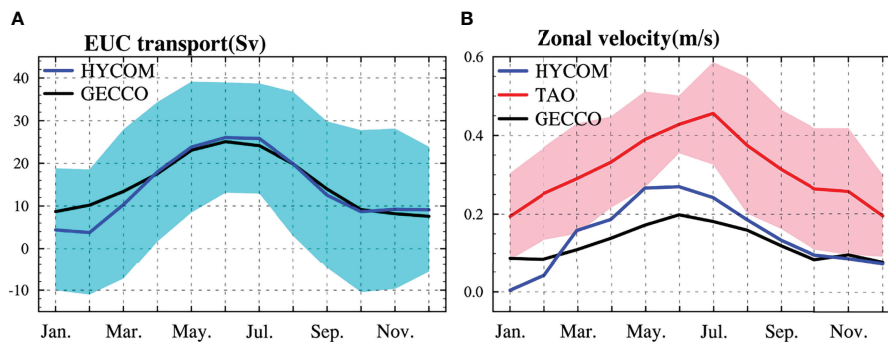

FIGURE 2 | **(A)** The annual cycle of EUCT (Sv) from GECCO and HYCOM, in which the blue shading marks the standard deviations of EUCT from HYCOM. Note that the EUCT from HYCOM is calculated in the area 3°S–3°N, 85 m–310 m. **(B)** The zonal velocity (m s^{-1}) at (165°E, 0°N) averaged in 100–300 m from TAO/TRITON observation, HYCOM, and GECCO, in which the pink shading marks the standard deviations of zonal velocity from TAO/TRITON observation. Note that the climatological zonal velocities of HYCOM and TAO/TRITON are averaged between 1994 and 2013.

where u is the monthly mean zonal velocity and the area 3°S–3°N, 87.5 m–310 m represents the EUC's core (**Figure 1**). Then, the adjoint sensitivities of J to the control variables (the wind stresses τ_x and τ_y specifically), i.e., $\partial J/\partial \tau_x$ and $\partial J/\partial \tau_y$, going backward in time (at 10-day interval) from July of the second year to January of the first year, are calculated. With a two-year climatological background of the adjoint model, the sensitivity results can reflect the impacts of both local and remote wind forcing on the EUCT. We also defined the target function J as the EUCT at 180°E and 140°W, and obtained similar results to that at 165°E, which will be discussed later.

3 RESULTS

3.1 The Modeled EUC and Its Variations

Due to lack of sectional observations of the EUC, we employ the eddy-resolving Hybrid Coordinate Ocean Model (HYCOM) reanalysis dataset (Bleck, 2002) to evaluate the GECCO-modeled EUC structure in terms of both the climatological state and seasonal anomalies of zonal velocity at 165°E (the selected target longitude). As shown in **Figure 1**, the modeled eastward-flowing EUC peaks in the subsurface layer, near 200 m, on the equator. The westward-flowing South Equatorial Current (SEC) south of 3°N and the eastward-flowing North Equatorial Countercurrent (NECC) near 5°N are also roughly reproduced, reflecting that GECCO is capable of reproducing the basic equatorial current system. However, due to the coarser resolution and the climatological air forcing, GECCO cannot reproduce the more refined features of these equatorial currents. For example, the EUC exhibits a broader scale and weaker magnitudes than that in HYCOM. In addition, the NECC is not distinctive as a single current but merges with the EUC to its northern side.

Whereas, the seasonal variability of the equatorial current system in the GECCO simulation is analogous to that in the HYCOM simulation. In boreal summer (May to July), the positive anomalies of modeled zonal velocity are distributed from the surface to 400 m within 3°S–3°N, leading to enhancement of the EUC and weakening of the SEC near the equator (**Figure 1B**). Meanwhile, at the latitudes of the NECC, the zonal velocity shows negative anomalies. In boreal winter (November to January), reversed velocity anomalies are exhibited, indicating the seasonal weakness of the EUC. In the other two seasons, the zonal velocity anomalies are also reversed. For example, in spring, the zonal velocity anomalies are negative from the surface to half the EUC depth (near 150 m) within 6°S–6°N but change to positive in the lower layer, which thus leads to a weak variation of the EUC. Comparably, HYCOM exhibits quite similar anomalies in the equatorial current system in four seasons but with some differences in the finer structures due to the higher resolution.

The seasonal variations of the EUC velocity at a single point and EUCT integrated over a certain meridional and vertical range are also compared with HYCOM and the direct velocity observations from the Tropical Atmosphere Ocean/Triangle

Trans-Ocean Buoy Network (TAO/TRITON) array (McPhaden and Taft, 1988) (**Figure 2**). Here, the EUCT is integrated along the section (3°S–3°N, 87.5–310 m) at 165°E, the time-mean transport in the region of EUC core (the green dashed-line box in **Figure 1**). It shows that the simulated EUCT peaks in June and drops in the winter months, consistent with the performance of HYCOM and previous studies (Philander et al., 1987; Johnson et al., 2002). In addition, compared with the TAO/TRITON observations, a similar seasonal variation of the EUC velocity is found but with weaker strength. As discussed above, this discrepancy may be attributed to the coarse resolution and climatological forcings. On the one hand, the coarse-resolution makes GECCO linear in its ocean dynamics, highly laying a good condition for its adjoint component to calculate the linear sensitivity. On the other hand, GECCO can roughly reproduce the basic structure of the EUC and its seasonal variations, providing the acceptable background state for the adjoint calculation. Therefore, GECCO is valid in exploring the linear sensitivity of the EUC to wind forcing.

3.2 Patterns of Sensitivities of EUC to Winds

For ease of explanation, July of the second year (the target month) is denoted as month 0, and the months ahead of a year are denoted as months –11 to –1. The two components of the monthly-mean adjoint sensitivities (i.e., $\partial J/\partial \tau_x$ and $\partial J/\partial \tau_y$) before month –11 are very weak and discarded; thus, only those from month –11 to month –1 are retained for analysis (**Figures 3**, **4**). The physical interpretation of the displayed sensitivity is that if the wind stress is disturbed with one standard unit over a 1°×1° grid box for one month, the EUCT in month 0 changes by the given sensitivity value. Therefore, a positive or negative sensitivity value indicates that the EUCT in month 0 increases or decreases if there is a positive change in the wind stress in the corresponding month and location. Some basic information is reflected in the sensitivity patterns.

First, sensitivities to both zonal and meridional wind stress are primarily confined to the tropical Pacific (15°S–15°N) except near the western boundary (20°S–30°N) in month –11 to –9. The meridional scopes extend broader in the western equatorial Pacific Ocean. The magnitudes of the sensitivities are generally strongest on the equator and decrease off the equator. More significantly, the adjoint sensitivity to zonal wind stress is much larger than that to meridional wind stress, suggesting the dominant effects of zonal wind forcing on EUCT variations. The structures indicate that it is the wind forcing in the tropical Pacific Ocean that has critical impacts on EUCT variations, in agreement with canonical views (e.g., McPhaden, 1981).

Second, the sensitivities exhibit highly symmetrical structures of the equator. For $\partial J/\partial \tau_x$, taking month –11 as an example, the symmetrical negative sensitivities extend equatorward from west to east, where the central axis is aligned with the equator, exhibiting a funnel-shaped pattern on both sides of the equator. The positive sensitivity, stuck in the middle of the funnel, is restricted in the western-to-central Pacific basin. Furthermore, outside of the negative sensitivity, positive phases
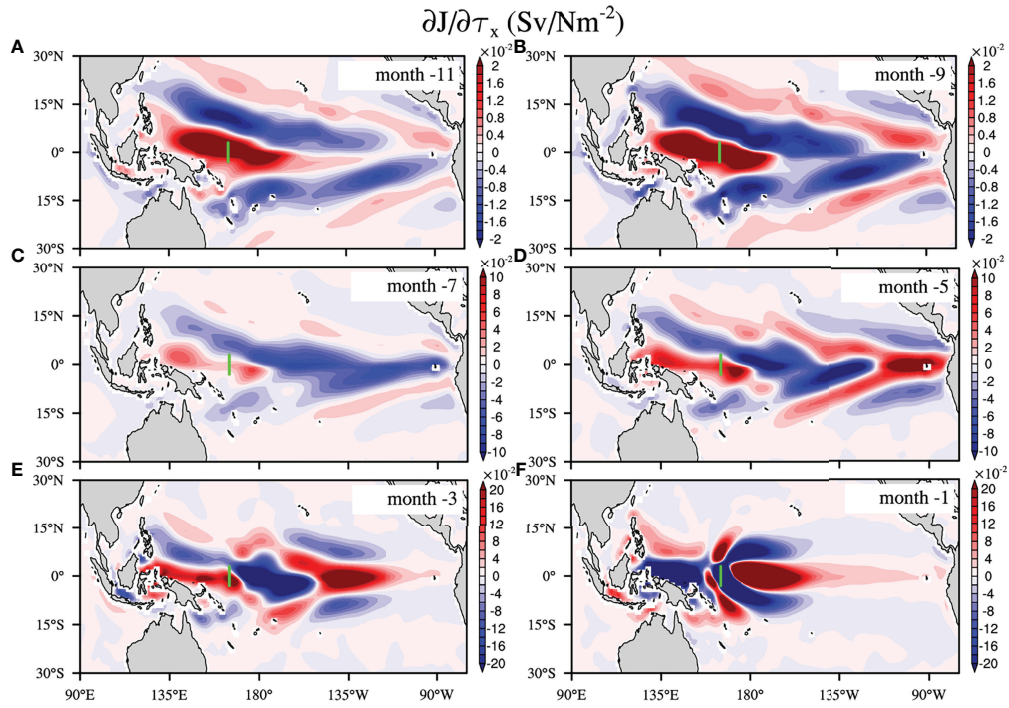
$$\partial J/\partial \tau_x \ (Sv/Nm^{-2})$$

FIGURE 3 | Monthly adjoint sensitivity (Sv/Nm^{-2}) of the EUCT in July to the zonal wind stress from previous 11 to 1 months (marked as **A–F**, respectively). Note that the representative values of color bars are gradually increasing with different months.
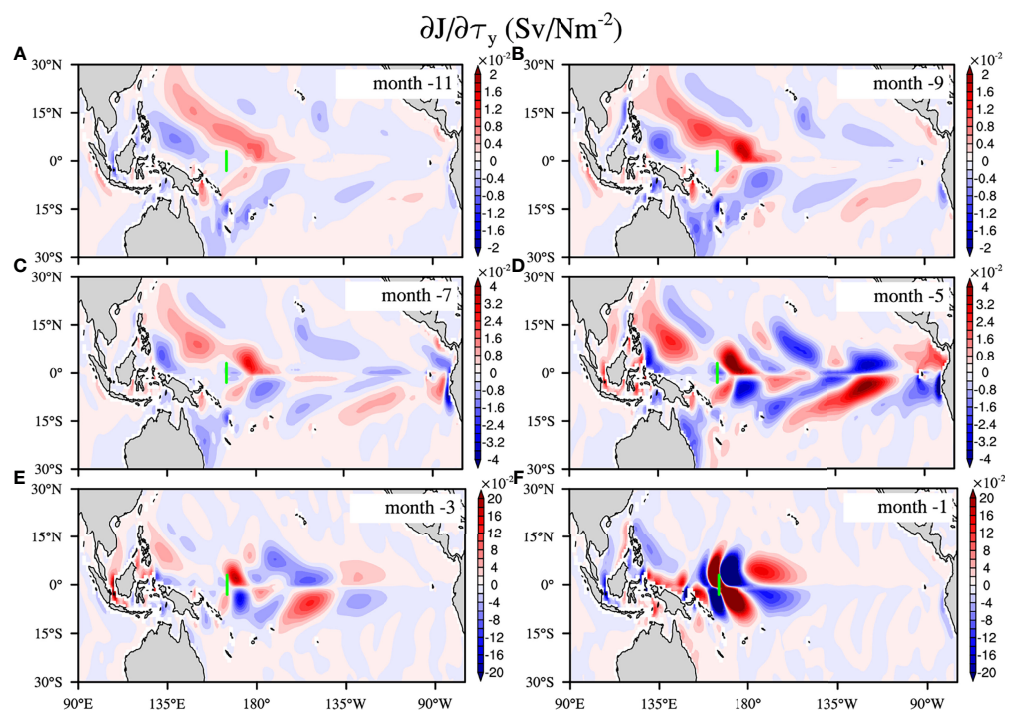
$$\partial J/\partial \tau_y \ (Sv/Nm^{-2})$$

FIGURE 4 | Same as **Figure 3**, but for meridional wind stress from previous 11 to 1 months (marked as **A–F**, respectively).

are symmetrically distributed but with much weaker strength, exhibiting wave-like patterns meridionally. Similar distributions are also found in other months. For $\partial J/\partial \tau_y$ equatorial symmetry also appears but with opposite signs between the north and south. The funnel-shaped pattern indicates that the nonzero wind stress curls of the optimal winds, as well as the nonzero divergence or convergence, may be critical for EUC variations.

Third, when approaching the target month, the magnitudes and the spatial scales of both sensitivities change accordingly. In detail, with more leading months, the sensitivities are distributed more remotely. At month –11, the meridional scope of the sensitivities extend nearly 20° off the equator but contract to nearly 10° after month –7. The zonal extents also contract from the whole Pacific Ocean in month –11 to the western basin near the target section (165°E) in month –1, indicating that local winds may be more critical for EUCT variations when they occur close to the target month. The magnitudes of the two sensitivities of $\partial J/\partial \tau_x$ and $\partial J/\partial \tau_y$ increase synchronously, indicating higher sensitivity to wind forcing in closer months. Obviously, the changing patterns in various leading months reflect that the wind perturbations in both remote and local regions are effective for EUCT variation. Both components display westward phase propagation from month –11 to month –1, implying that equatorial wave processes may be used to explain how sensitive wind affects the EUC.

As a whole, the adjoint sensitivity provides precise insight into where, when, and what wind perturbations can enhance the EUC. Specifically, the expected wind perturbation manifests as a funnel-shaped and highly symmetric pattern in the tropical Pacific Ocean, and propagates westward along with time. Taking advantage of the adjoint model, the derived specific pattern of optimal winds should be more effective than any other pattern of winds in inducing EUC variations. In the following subsection, we investigate how the specific sensitive winds impact the EUC. Note that because the adjoint model solves a set of equations that are linearized around the background ocean state, adjoint-derived sensitivities are a linear approximation to the nonlinear response of ocean state (Verdy et al., 2014). In our study, the linearity assumption is shown to hold well and is demonstrated by the nonlinearity check in wind perturbation experiments with different perturbation ratio (**Figure S3**).

3.3 Impacts of the Sensitive Winds

3.3.1 On the EUC Along the Target Section (165°E)

Here, experiments are conducted by superimposing sensitivity-like wind perturbations in various leading months. In the following, we describe the procedure for producing sensitivity-like wind perturbations. First, to constrain the upper magnitudes of the wind perturbations, the maximum wind velocity perturbation is set to be proportional to the maximum wind velocities by a factor of δ and prescribed at the grid point of the maximum $|\partial J/\partial \tau_x|$. Then, the zonal and meridional perturbations of wind (ΔU, ΔV) at each grid can be written as:

$$\Delta U = \frac{\partial J/\partial \tau_x}{\max(|\partial J/\partial \tau_x|)} \cdot \delta \cdot \max(|U_0|), \tag{7}$$

$$\Delta V = \frac{\partial J/\partial \tau_y}{\partial J/\partial \tau_x} \cdot \Delta U, \tag{8}$$

where U_0 is the original zonal wind velocity in the corresponding months at 30°S–30°N. Finally, the wind perturbations at all the model grids, with the same patterns for the adjoint sensitivities, are prescribed by the factor δ (Those wind perturbations are called 'optimal winds'). Here, δ is set to 20% for all experiments. Although it is the wind velocity vector that is perturbed, the wind stress vector perturbation exhibits almost the same pattern (not shown).

Considering the various sensitive wind patterns in the leading months, to distinguish the effectiveness of both the remote and local sensitive wind forcing, three numerical experiments are conducted, by superimposing the sensitivity-like wind perturbations on the original wind field at months –11, –6, and –2. Those three experiments are representative of the long-term, medium-term, and short-term wind forcings. As shown in **Figure 5**, these wind perturbations show major funnel-like patterns with distinctive curls along the equatorial Pacific Ocean. Note that those wind forcings only drive the ocean for one month, and then, the model is integrated forward under the same configuration as the background simulation till the end.

To quantify the impacts of the sensitivity-like wind perturbation, the changes in EUCT as a function of time are calculated by equation (6) (figure not shown). The monthly mean EUCT decreases instantly after the wind perturbations and increases during the following months. At the target month (month 0), the EUCT anomalies are all positive for the three experiments, meaning the EUCT is enhanced by the wind perturbations. The increased EUCT at month 0 in the experiment of month –11 is smaller than that in the other two situations, which may be due to the weaker amplitudes of the sensitivity-like wind perturbations (**Figure 5**) and longer response period, and the nonlinearity may also be a factor of the relatively weak response of EUC to the optimal perturbation on the wind fields 11 month ago. The different intensities of the increases in EUCT at month 0 also indicate the various effects of remote and local wind forcing on the EUC variations. The results here verify that the sensitivity-like structures in the wind perturbations can indeed increase the EUCT at the target section and target month as set in the cost function, coinciding with the physical meanings of the adjoint sensitivity. This also, in turn, validates the correctness of the sensitive wind patterns achieved by the adjoint model in GECCO.

3.3.2 On the EUC at Basin Scale and in the Right Layers

As introduced in the Introduction, the EUC is a basin-wide subsurface current flowing eastward along the equatorial thermocline covering the whole Pacific Ocean. Therefore, driving the enhancement of the EUCT in a single section (165°E) does not necessarily demonstrate that the sensitive
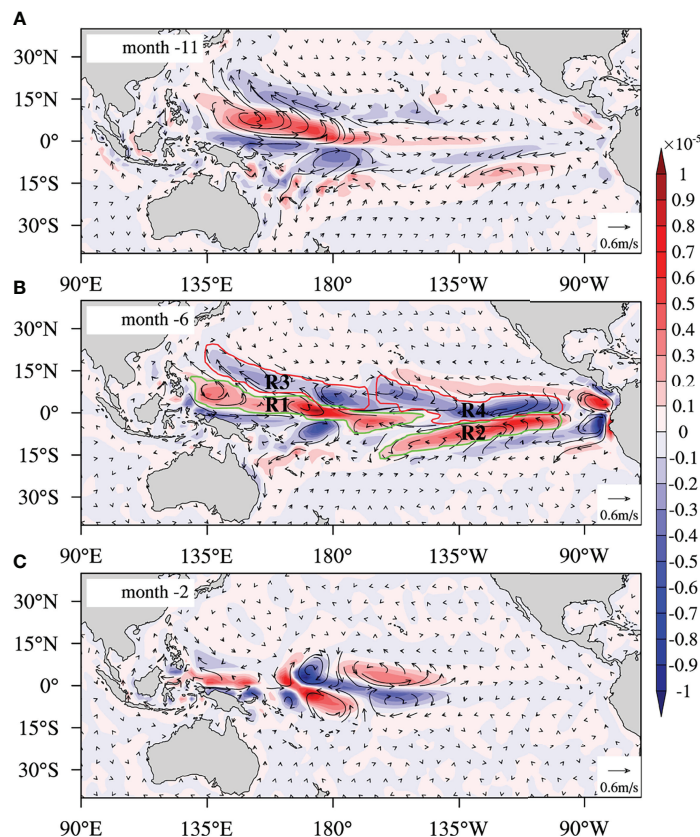
FIGURE 5 | Horizontal distributions of the sensitivity-like wind velocity perturbations (vectors; m s^{-1}) and the corresponding wind curl (color shading; s^{-1}) at **(A)** month –11, **(B)** month –6, and **(C)** month –2. The outlined regions in **(B)** indicate the independent perturbations used to investigate the dynamical mechanisms in subsection 3.4.3.

wind perturbations may also lead to the enhancement of EUC at the basin scale. To further investigate whether the EUC can also be enhanced in the basin scale and the right subsurface layers by those sensitivity-like wind perturbations, we show the horizontal distribution of the resulting zonal velocity anomalies averaged over the EUC depths, i.e., potential density layers $\sigma_\theta = 23.0$ to 26.2 (Johnson et al., 2002), of the three experiments (**Figures 6–8**). Here the zonal velocity anomaly is defined as the difference between the perturbed state caused by the sensitive wind and the unperturbed state.

The responses to remote and local wind forcings are different. The wind perturbations at month –11 (i.e., the long-term wind, **Figure 6**) and month –6 (i.e., the medium-term wind, **Figure 7**) are examples of remote wind forcing, while that at month –2 (i.e., the short-term wind, **Figure 8**) is an example of local wind forcing. As responses to the remote wind forcing (**Figures 6, 7**), the resulting subsurface zonal velocity anomalies in the following first several months of the wind perturbations exhibit a basin scale and nearly symmetrical distribution about the equator over the entire equatorial Pacific Ocean; meridionally, the anomalous velocities can reach 20°S–20°N; however, the meridional extension shrinks along with time. Approaching month 0, the structures of the eastward velocity anomalies are relatively

simple: they extend from the western boundary to nearly the eastern boundary of the equatorial Pacific, covering the whole basin; they are confined to approximately 3°S–3°N in the western Pacific Ocean but gradually expand to a slightly wider meridional range eastward. This demonstrates that the remote wind forcing-resulting EUC enhancement is indeed at the basin scale.

We further confirm this feature with the zonal and meridional sections of the zonal velocity anomalies in the target month for the two experiments (**Figures 9A, B, D, E**). In the target month (month 0) and the target section (165°E), the enhanced EUC (i.e., positive zonal velocity anomalies) is primarily located at EUC depths, which are centered at 150 m, and rang between depths of 100 and 300 m; in addition, they are primarily confined within 3°S–3°N (**Figures 9A, B**), the exact positions of the EUC. From west to eastward, the enhancement is also mainly confined in the thermocline (i.e., between $\sigma_\theta = 23.0$ and 26.2; **Figures 9D, E**), approximately coinciding with the right layers of the EUC in the equatorial Pacific. Therefore, it confirms that the zonal velocity response to the sensitive wind takes place in the right subsurface layer and the basin scale rather than only at the target section of 165°E. Notably, we also conduct numerical experiments driven by remote sensitivity-like wind perturbations in other months (including months –11 to –4) and achieve similar results.
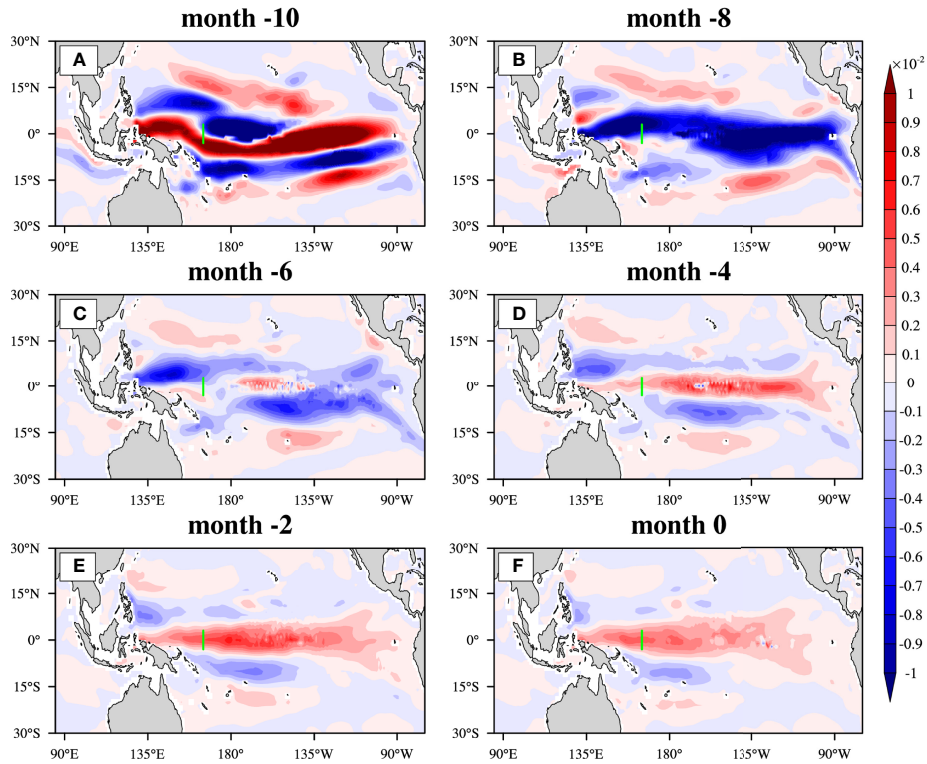
FIGURE 6 | Evolution of the zonal velocity anomalies (m s^{-1}) averaged between σ_θ = 23.0 and 26.2 from previous 10 months to the target month (marked as **A–F**, respectively) due to the sensitivity-like wind velocity perturbation at month –11. The zonal velocity anomaly is defined as the bias between the unperturbed state and the perturbed state caused by the sensitive wind. The target section is marked with a green line.

However, when the wind perturbs the ocean near the target month (i.e., the local and short-term wind), the responses of the zonal velocity are different. For the experiment driven by the sensitivity-like wind perturbations at month –2 (**Figure 8**), the resulting zonal velocity anomalies evolve as wave-like fluctuations along the equator. In the target month, the EUC velocity anomalies are positive only in the western equatorial Pacific Ocean around the target section; eastward, they manifest as a negative-and-positive alternating pattern. This means that the EUC enhancement driven by the local wind occurs only near
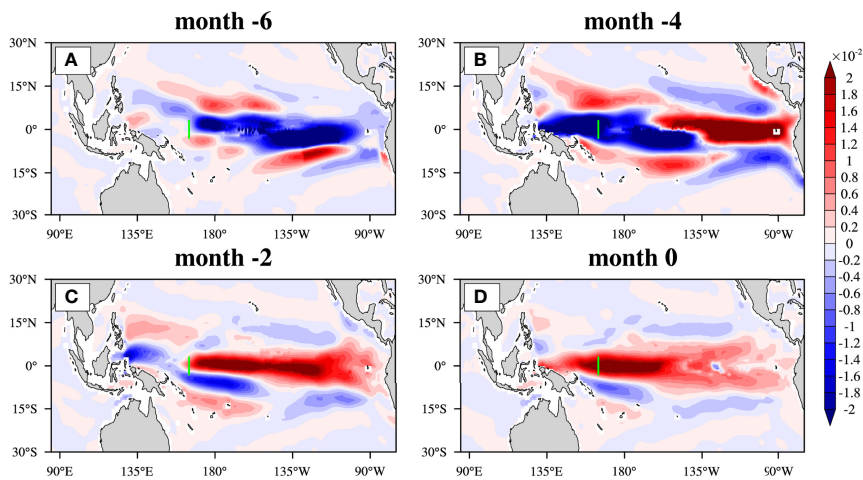

FIGURE 7 | Same as **Figure 6** but due to the sensitivity-like wind velocity perturbation at month -6 and **(A–D)** represent different previous months.
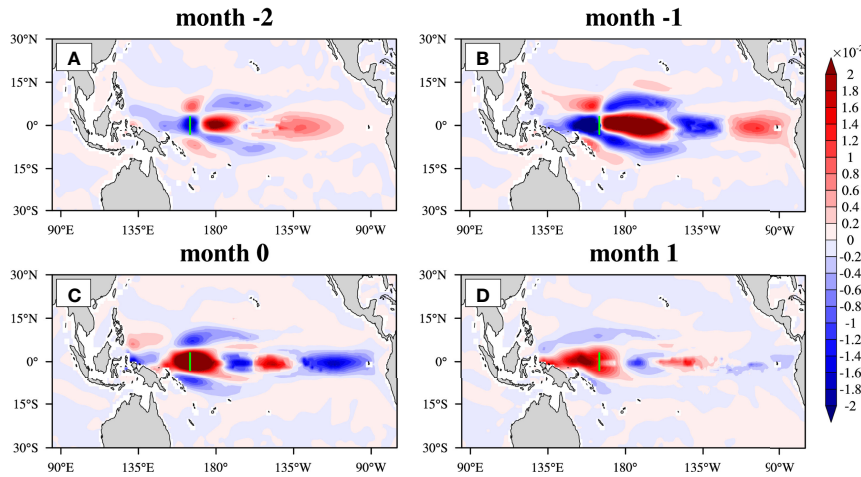
FIGURE 8 | Same as **Figure 6** but due to the sensitivity-like wind velocity perturbation at month −2 and **(A–D)** represent different previous months.

the target section. As further shown in the zonal and meridional sections (**Figures 9C, F**), the zonal velocity anomalies are positive and centered near 120 m in the 165°E section; however, they change to negative in the eastern equatorial Pacific along the equatorial thermocline. This clearly demonstrates that the EUC enhancement to the sensitivity-like wind perturbation at month −2 does not occur along the basin-scale EUC axis; rather, it is confined to the region of the target section. In addition, with additional experiments, it is found that when the lead period of the wind forcing is less than 4 months, the EUC responses show a pattern similar to that at month −2 (figures not shown). This demonstrates that the local wind

(specifically, preceding less than 4 months) cannot induce basin-scale EUC variation; rather, it can induce only local EUC variation.

In other words, when the lead time of wind forcing is 11 to 4 months (medium to long term), the wind can modulate the EUC variations at a basin scale. This is because, since the EUC is a consecutive basin-scale current, the initial oceanic responses need time (at least 4 months) to adjust to fit the EUC structure at a basin-wide scale. Comparatively, a sensitive wind leading by less than 4 months (local and short-term) can result only in a local variation of the EUC, because the response period is too short to generate a wide-range variation.
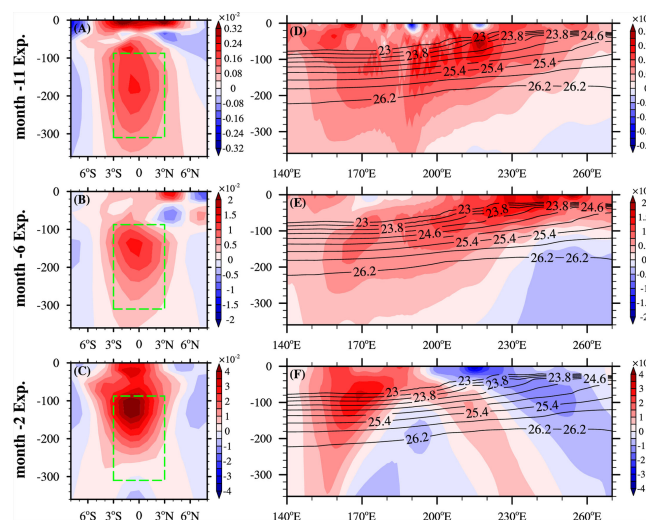

FIGURE 9 | **(A–C)** Meridional sections at 165°E and **(D–F)** zonal sections averaged over 3°S–3°N of the zonal velocity anomalies (m s^{-1}) at the target month (i.e., month 0) due to the sensitivity-like wind perturbations at month −11, month −6, and month −2, respectively. The contours in **(D–F)** represent potential densities with an interval of 0.4 kg m^{-3}.
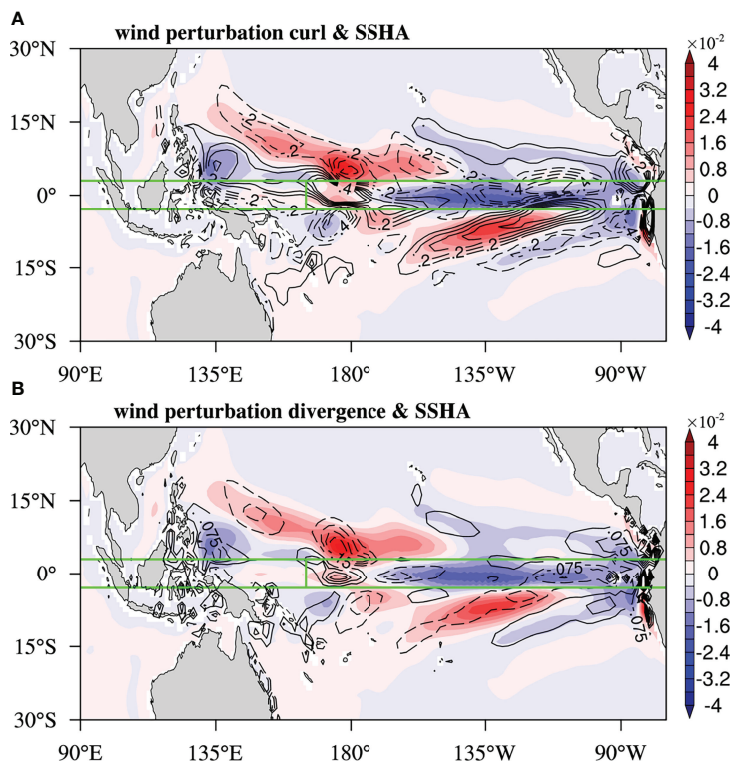
FIGURE 10 | (A) Color shading represents the response of SSHA (m) to sensitive wind velocity perturbation at month −6, and the contours denote the corresponding wind velocity perturbation curl (10^{-5} s^{-1}). **(B)** same as **(A)**, but the contours represent the corresponding wind perturbation divergence. The contour interval is 01×10^{-5} s^{-1} in **(A)**, and 0.0375×10^{-5} s^{-1} in **(B)**. In addition, the level green lines correspond to ±3°, and the vertical green line represents the target section.

3.4 New Mechanisms for Wind-Driven EUC Variations

3.4.1 The Kelvin Wave-Driven Mechanism

In equatorial dynamics, sea surface height anomalies (SSHAs) are closely associated with thermocline variations and have been widely used to track the propagation of equatorial waves (e.g., Delcroix et al., 1991; Bosc and Delcroix, 2008; Chen et al., 2015; Chen et al., 2019; Lyu et al., 2020). Generally, positive SSHAs can characterize downwelling oceanic wave signatures due to water convergence in the upper layer, whereas negative SSHAs can characterize upwelling oceanic wave signatures due to water divergence in the upper layer (Bosc and Delcroix, 2008). In particular, downwelling equatorial Kelvin waves (DKs) and upwelling equatorial Rossby waves (URs) are associated with eastward current anomalies at the equator. Analogously, upwelling equatorial Kelvin waves (UKs) and downwelling equatorial Rossby waves (DRs) are related to westward current anomalies at the equator.

To illustrate the underlying dynamical mechanisms for the sensitivity-like wind perturbation-induced EUC variations, in the following, we show the time evolutions of the resulting SSHA and subsurface zonal velocity anomalies driven by wind perturbation at month −6. At month −6, the significant wind anomaly just north of the equator at approximately 180°E, which

has a negative wind curl, induces a region of positive SSHA (**Figure 10A**); this SSHA is associated with anticyclonic circulation, manifesting as a downwelling Rossby wave (denoted DR1 in **Figure 11A**). Another downwelling Rossby wave south of the equator between 160°W and 110°W (denoted as DR2 in **Figure 11A**) is generated by the corresponding wind curl therein (**Figure 10A**). In the following month, the DRs propagate westward, leading to a remarkable westward current anomaly at 165°E at the equator (**Figure 11A**). In the evolution to month −3, the western parts of both DR1 and DR2 approach the western boundary and start to be reflected as a downwelling Kelvin wave (DK1) that travels eastward along the equator and is associated with eastward zonal currents (**Figure 11B**). In the following months, while the old Kelvin wave propagates eastward, new Kelvin wave signals are continuously generated near the western boundary by the reflection of the two Rossby waves, forming a basin-scale Kelvin wave-like structure with a basin-scale zonal current anomaly (**Figures 11C, D**). The eastward current anomaly contributes to the basin-wide EUC increase.

These processes indicate that the specific equatorial Kelvin waves can be considered as a driving mechanism for the EUC variation at the basin scale. Note that the 'Kelvin wave-like structure' mentioned in this subsection does not necessarily
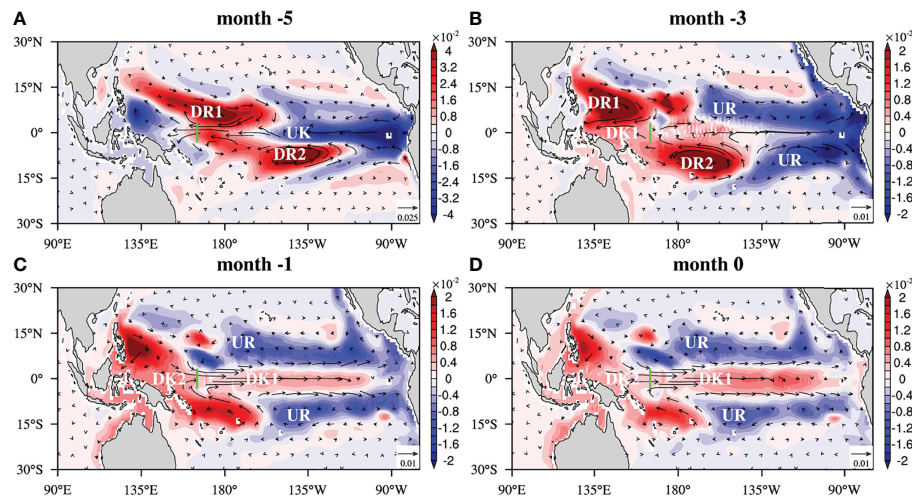
FIGURE 11 | Time evolutions of both the SSH anomalies (color shading; m) and zonal velocity anomalies averaged between σ_θ = 23.0 and 26.2 (vectors: m s^{-1}) at **(A)** 5 month, **(B)** 3 month, **(C)** 1 month previously, and **(D)** the target month in response to the sensitivity-like wind velocity perturbations at month –6. UK, DK, UR, and DR denote an upwelling Kelvin wave, a downwelling Kelvin wave, an upwelling Rossby wave, and a downwelling Rossby wave, respectively. Note that the representative values of the color bars and reference vectors gradually decrease with different months. And the target section is marked as the green line.

denote a single Kelvin wave but can consist of a series of Kelvin waves. For example, at month 0, the oldest Kelvin wave (DK1) is centered at the equatorial central Pacific Ocean, while a successive Kelvin wave (DK2) is centered still near the western boundary (**Figure 11D**).

3.4.2 The Rossby Wave-Driven Mechanism

Apart from the Kelvin wave-driven mechanism, the Rossby wave-associated circulation anomalies can also be regarded as a mechanism for the EUC variations. At month –6, a negative SSHA (i.e., an upwelling Kelvin wave, denoted the UK in **Figure 11A**) is generated by the equatorial easterly anomaly (which has negative divergence) within ±3° in the central-eastern Pacific Ocean (between 150°W and 80°W, shown in **Figure 10B**). In the following month, the UK continues to propagate eastward (shown in **Figure 11A**). Then, from months –5 to –3, the UK reflects at the eastern boundary to generate two equatorial URs between 170°W and 80°W. At month 0, the cyclonic circulations associated with the two URs at the equator display an eastward current anomaly near the equator, promoting a nearly basin-wide (mostly in the central to eastern equatorial Pacific) EUC increase as well.

Therefore, the basin-wide EUC variations are verified to be modulated by basin-wide equatorial Kelvin waves and Rossby waves. The Kelvin wave- and Rossby wave-driven mechanisms complement the canonical EPGF mechanism. If both mechanisms take effect, the waves usually manifest as a meridional negative-positive-negative SSHA pattern between 15°N and 15°S, as shown in the central-eastern tropical Pacific in **Figure 11D**. In particular, the upwelling Rossby waves correspond to the poleward meridional pressure gradient force (MPGF), indicating that the MPGF at the equator can be an indicator of EUC variation. By simplifying the primitive

equations using scaling analysis, Chen et al. (2018) showed that the northward pressure gradient is important to EUC formation, confirming the viewpoint of the Rossby wave mechanism in our study. However, under the downwelling Kelvin wave-driven mechanism, the ZPGF does not need to be eastward; rather, it can be toward both east and west from the high-pressure center of each Kelvin wave based on the dynamics of a typical equatorial Kelvin wave (Boyd, 2018).

Notably, a similar final pattern of combined equatorial waves with an ultimate increment of the EUC can also be found in other experiments, with the original Rossby and Kelvin waves excited by sensitivity-like wind perturbations leading by no less than 4 months (figure not shown). Generally, the horizontal scale of the original responding waves is not as large as that of the basin; however, during their propagation and reflection, they usually adjust into a basin-scale pattern, resulting in an eastward current anomaly that eventually extends across the whole Pacific Ocean. Note that the equatorial waves are associated with the meridional or zonal pressure gradient anomalies, and circulation anomalies as well, thus these waves are not part of the EUC. And although the scale of waves in our study is large, they still have the characteristics of propagation, thus waves and circulations can be separated essentially. However, when the variations of both the EUC and waves happen on the basin scale, the waves and the circulations are not separated easily, particularly from *in-situ* observations.

The results indicate that the timing and original structure of the wind play crucial roles. This is because a specific wind pattern is required to generate the proper Rossby waves and Kelvin waves at the equator, both of which need appropriate time to form a basin-scale structure that favors the enhancement of the EUC. As long as the wind structure meets such a condition, the resulting Kelvin and Rossby waves will eventually lead to basin-
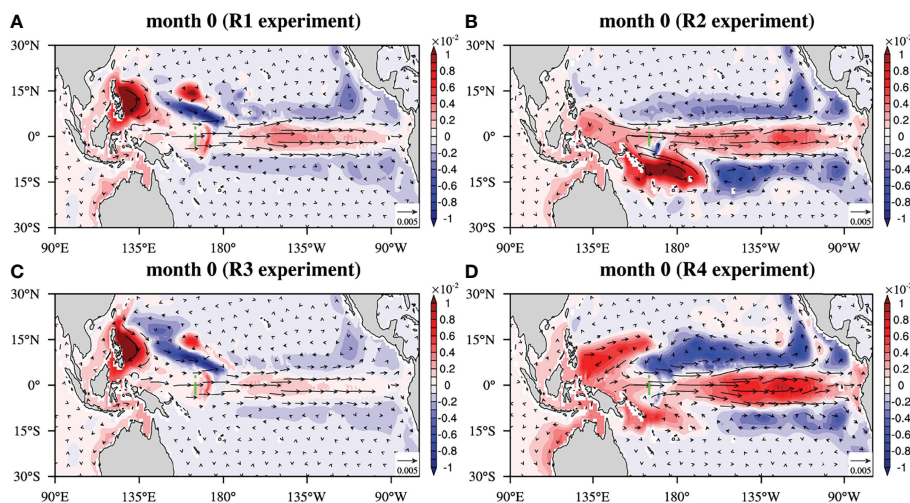
FIGURE 12 | Same as **Figure 11**, but the responses of SSHA (color shading; m) and zonal velocity anomalies (vectors: m s^{-1}) at month 0 due to the regional sensitivity-like wind perturbations **(A)** R1, **(B)** R2, **(C)** R3, and **(D)** R4 (shown in **Figure 5B**) exerted at month –6.

scale EUC enhancement. This is why we obtain the funnel-shaped structure of sensitivity and why the sensitive winds vary with location and month. In other words, the EUC varies due to equatorial wave-associated zonal currents that are generated by winds with specific patterns, locations and timing. This mechanism highlights the importance of the spatial pattern of the wind perturbations to induce the Rossby waves and Kelvin waves, which are responsible for the EUC increase, and the waves are associated with the wind stress curl off the equator and wind divergence at the equator.

3.4.3 Kelvin and Rossby Waves Caused by Regional Wind Perturbations

As mentioned above, the sensitivity-like wind perturbations as a whole indeed increase the EUC at the target month at the basin scale. However, the real wind cannot conform to the integral pattern of the sensitivity-like wind perturbations. Therefore, it would be interesting to know whether regional wind perturbations with the sensitive pattern are also able to cause EUCT responses *via* Kelvin and Rossby wave-driven mechanisms. To do so, we select the anticyclonic and cyclonic wind perturbations as regional independent winds. Taking the wind perturbations in month –6 as an example, we conduct additional experiments that are driven by the monthly climatological wind superimposed by the four independent wind perturbations (shown in **Figure 5B**, denoted as R1–R4).

As shown in **Figure 12**, the SSHA at month 0 driven by the four independent wind perturbations displays a meridional negative-positive-negative pattern from 15°N to 15°S in general, similar to that driven by the integral wind perturbations (**Figure 11D**), which results in basin-scale EUC enhancement. During the evolution process, the wave signatures of the equatorial DK and the equatorial UR propagate in a similar way (not shown). The differences lie in the amplitudes of

the EUC variation caused by the independent regional wind perturbations, which are weaker than those induced by the integral perturbations, due to less initial wind forcing. Overall, the experiments demonstrate that the sensitive wind perturbations derived by the adjoint method can increase the EUC not only jointly but also separately. Therefore, if realistic wind anomalies exhibit a similar pattern with any independent components, the EUC could be consequently enhanced.

3.5 Results at Other Sections (180°E and 140°W)

In the above sensitivity calculation, we set 165°E as the target section and hence the target function *J*. What about other sections? Would setting a different longitude as the target section change the conclusions? Here, we demonstrate that this selection does not change the revealed mechanisms above. We set the target EUCT at 180°E and 140°W and repeated the above sensitivity calculation and experiments. The sensitive wind exhibits a symmetrical ribbon-shaped pattern (**Figure 13**), similar to that for the 165°E section (**Figure 5B**). In detail, the easterly wind anomaly is primarily located in the central-eastern Pacific Ocean along the equatorial band, and the westerly wind anomaly is located in the western Pacific Ocean along and just south of the equator. The meridional range of the sensitive wind is slightly narrower for the 180° section experiment (within 10°S–10°N) than for the 165°E section experiment. The sensitive winds are also associated with specific patterns of wind curls (**Figure 13**) and divergences (not shown), causing the generation of Rossby and Kelvin waves.

During the following months, the anomalous oceanic signals propagate in a way similar to that described for the 165°E case (**Figure 14**). Eventually, at month 0, the meridional negative-positive-negative pattern of SSHA is formed in the central to eastern tropical Pacific Ocean, meaning that both the Rossby and
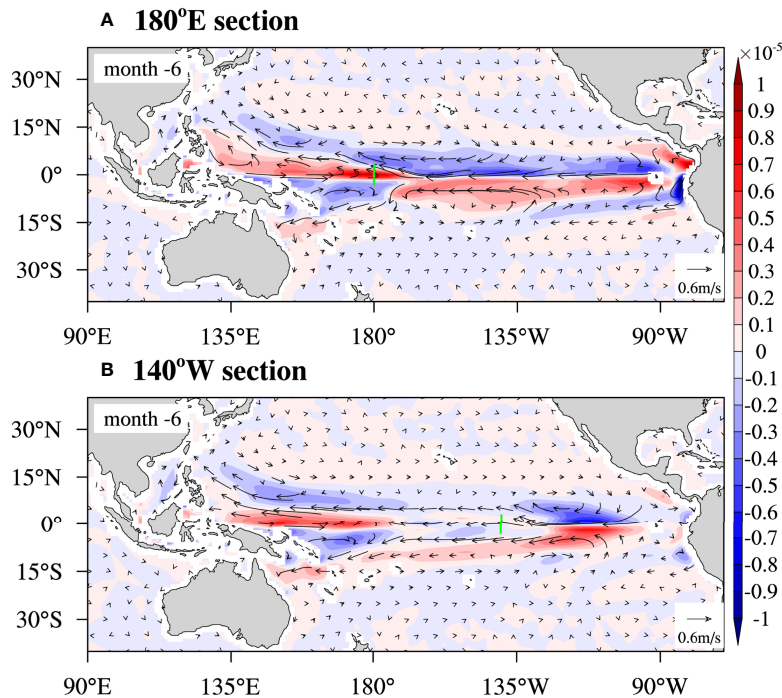
FIGURE 13 | Horizontal distributions of the sensitivity-like wind velocity perturbations (vectors; m s^{-1}) and corresponding wind curl (color shading; s^{-1}) at month −6. **(A)** and **(B)** represent the target sections at 180°E and 140°W, respectively.

Kelvin wave-driven mechanisms are responsible for the EUC increase therein; however, in the western equatorial Pacific, the Kelvin wave-driven mechanism dominates, manifesting as a high SSHA to the western boundary. In contrast, the westward propagation of URs (i.e., equatorial negative SSHAs) seems to depend on the locations of the target section. For example, for the 140°W case, the URs are mainly distributed in the eastern basin of the target section, where the Rossby wave-driven mechanism dominates.

In summary, regardless of the longitude of the target section, a basin-scale EUC variation can always be obtained by the adjoint-derived sensitive winds as long as the winds lead by more than 4 months. It should be caused by the zonal continuity of the EUC.

4 SUMMARY AND DISCUSSION

It has long been thought that the primary driving factor for the EUC maintenance and variation is the easterly trade winds *via* the zonal pressure gradient force (ZPGF). Recently, Lyu et al. (2020) found that variation of the EUC in the western Pacific is controlled by a large-scale circulation that is associated with a Rossby wave initiated approximately half a year before in the central-eastern Pacific basin. This implies that the structures and time of the winds and the underlying wind-driven mechanisms need to be systematically investigated. In the present study, using

the adjoint-sensitivity method based on GECCO synthesis, we obtain the spatially and temporally varying sensitive winds that can most efficiently influence the EUC variations and provide new driving mechanisms.

At various leading times, the adjoint sensitivities (optimal winds) are confined to the tropical oceans (15°S–15°N) and exhibit a funnel-shaped pattern with high symmetry around the equator. From month −11 to month −4, the adjoint sensitivity is mainly concentrated in the central-eastern Pacific Ocean, showing a remote wind effect, while for shorter lead times, i.e., months −3 to −1, the majority of sensitivity is confined to the western equatorial Pacific Ocean near the target section 165°E. The remote winds (at months −11 to −4) can lead to EUC variations at the basin scale, while the local winds lead to only local EUC variations.

Based on the above sensitive winds, we derive new mechanisms for EUC variations, i.e., basin-scale equatorial Kelvin wave-driven and Rossby wave-driven mechanisms. The wind-forced initial equatorial Kelvin waves, Rossby waves, and the reflected waves at both the western and eastern boundaries superimpose with each other and lead to EUC variations. Specifically, the URs and DKs, associated with the eastward current anomalies at the equator, are responsible for the EUC variation. When the travel time is longer than 4 months, the waves can form a negative-positive-negative SSHA pattern between 15°S and 15°N in the central-eastern tropical Pacific, indicating the influence of both mechanisms. The presence of a
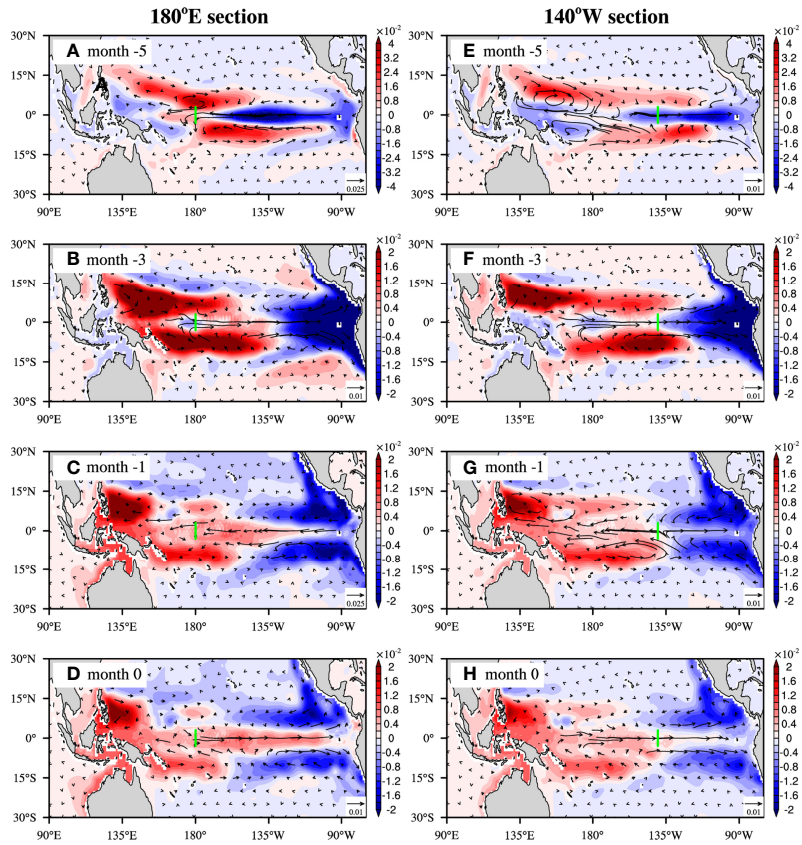
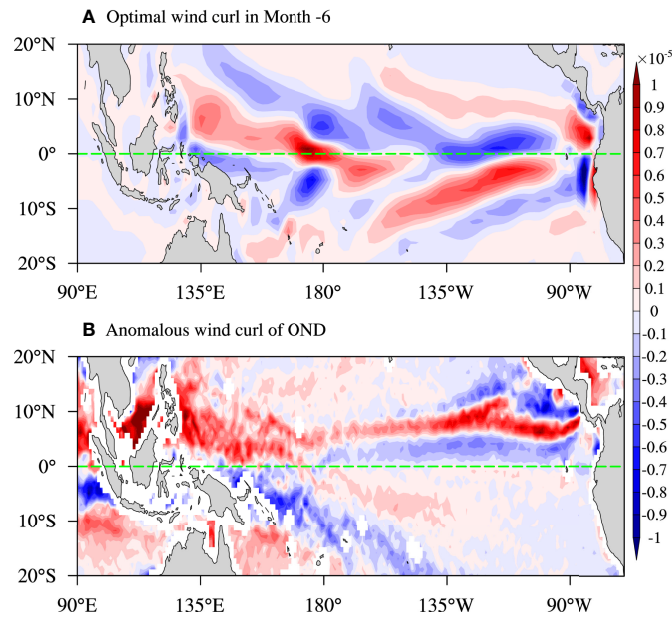**FIGURE 14** | Same as **Figure 11** but for the target sections at **(A–D)** 180°E and **(E–H)** 140°W.

FIGURE 15 | The comparison of the **(A)** sensitivity-like wind curl (s^{-1}) at month–6 and **(B)** the wind curl anomalies averaged at winter months (October to December) during 2000-2008 from the QuikSCAT satellite data.

positive SSHA in the western equatorial Pacific indicates the dominance of the Kelvin wave-driven mechanism. These mechanisms can be regarded as complementary to the canonical ZPGF mechanism for basin-scale EUC variation.

In the present work, the adjoint sensitivity of wind forcing has clearly displayed the spatial patterns, locations, and leading times of the critical wind perturbations, which can excite the EUC increase at a basin scale rather than a particular section only. The evolutions of oceanic responses indicate that the wind-driven Kelvin and Rossby waves are associated with the basin-scaled EUC changes. In addition, the results for the cost function at the other sections also reveal the similar physical regime, enriching our conclusions for the total Pacific EUC. Therefore, the three problems raised in the Introduction have been solved. However, we note that the aforementioned optimal sensitive winds are obtained by the adjoint-sensitivity method; hence, the winds are ideal rather than real. The advantage of the obtained ideal winds is that they can clearly and simply explain the underlying dynamical mechanisms, while it is difficult to strip the driving processes and hence the mechanism from the real complex winds. Therefore, the identified new wind-driven mechanisms provide a clear theoretical basis for the EUC variation studies. In addition, we demonstrate that the individual components of the whole optimal wind pattern (i.e., the R1–R4 parts) can separately result in basin-scale EUC variations, indicating that, if the real winds partly fit the ideal winds, the EUC may still be influenced. Here, we quickly test if it is instructive to explain the significant seasonal variations of the EUC, which is usually strongest in June–July (**Figure 2**). We assume that the basin-scale enhancement of EUC in June–July is on average caused by equatorial winds of 6–8 months before, i.e., the winds of October–December in the last year. We calculate the climatological anomaly of wind curl of October–December using the Quick Scatterometer (QuikSCAT) satellite data and show its comparison with the sensitivity-like wind curl at month −6 in **Figure 15**. It displays that, the realistic wind anomaly exhibits a similar distribution at the tropic ocean, especially at the northern equator, despite of the inevitable differences on the southern side. Specifically, the negative wind curl along the central-eastern Pacific Ocean is consistent with the R4 component, and positive values at the western Pacific Ocean fit with R1 partly. It indicates that those regional winds may be (partly) responsible for the EUC enhancement during June-July. Thus, the adjoint-sensitivity patterns provide a benchmark for searching the potentially influential winds that may be responsible for the EUC variations. In this sense, the results provide useful guidance for the possible wind-driven processes of the seasonal to interannual variations of the EUC.

Both the obtained Kelvin wave-driven mechanism and the Rossby wave-driven mechanism have implications for explaining some of the observed phenomena of the EUC. First, even though the EUC is considered as a basin-scale continuous eastward current forced by the EPGF, it is often observed that there is no basin-scale EPGF from west to east; rather, the ZPGF can be negative in some sections and positive at other sections (Johnson et al., 2000). The canonical ZPGF does not explain this phenomenon. In contrast,

this may be explained by the Kelvin wave-driven mechanism because the ZPGFs associated with the Kelvin wave are opposite on the sides of the pressure center of the wave, while the associated zonal currents maintain a consistent direction. Second, the Rossby wave-driven mechanism, which is associated with the meridional pressure gradient, may be used to explain the observed meridional shift of the EUC, or the asymmetry feature of the EUC about the equator. For example, Lyu et al. (2020) found from observations that the strengths of the EUC at different latitudes (142°E, 1°S), (142°E, 0°) and (140°E, 2°N) vary differently; the monthly meridional shift of the EUC core was also observed (Johnson et al., 2002, their **Figure 8**). The asymmetric nature of the EUC was simulated by a simple ideal-fluid model in the case of asymmetric wind forcing (Huang and Jin, 2003). This phenomenon may also be explained by the different arrival times or strength of Rossby waves on both sides of the equator, though detailed studies are required to confirm these hypotheses.

Finally, we would like to show that the linear wave dynamics could be the right one because the adjoint sensitivity is calculated based on the tangent linear ocean dynamics. To prove that the adjoint sensitivity is confined dynamically to the linear dynamics, we also use a highly non-linear system with a horizontal resolution of 1/6°×1/6°, the adjoint-based TOOSSE (Two Oceans One Sea State Estimate; Wang et al., 2021), to calculate the EUCT's sensitivity to wind forcing. The resulted patterns are very similar to GECCO (see **Figures S4, 5**). It indicates that the same (linear) wind-driven mechanisms for EUC variations are contained in both linear and nonlinear systems. It means that GECCO can be used to derive those underlying mechanisms. Of course, GECCO cannot be used for deriving nonlinear mechanisms (such as Mesoscale eddy processes) for wind-driven EUC variations.

DATA AVAILABILITY STATEMENT

The raw data supporting the conclusions of this article will be made available by the authors, without undue reservation.

AUTHOR CONTRIBUTIONS

CL, JW, and FW contributed to conception and design of the study. AK contributed particularly to adjoint sensitivity conception and techniques. All authors contributed to the article and approved the submitted version.

FUNDING

SUPPLEMENTARY MATERIAL

The Supplementary Material for this article can be found online at: https://www.frontiersin.org/articles/10.3389/fmars.2022.908939/full#supplementary-material

Supplementary Figure 1 | The difference between adjoint sensitivity and traditional forward perturbation sensitivity from Jones et al. (2018).

Supplementary Figure 2 | Schematic diagram of the relationship between the adjoint model and nonlinear model.

Supplementary Figure 3 | Responses of EUCT in July to the wind perturbations with various magnitudes at month –6, *via* varying the wind perturbation ratio from -0.35 to 0.35 at an interval of 0.1.

Supplementary Figure 4 | Adjoint sensitivity (Sv/Nm^{-2}) of the EUCT at 142°E in July of the second year to monthly zonal wind stress from previous 11 to 1 months (marked as **A–F**, respectively) derived by GECCO.

Supplementary Figure 5 | Same as **Figure S4**, but derived from TOOSSE from previous 11 to 1 months (marked as **A–F**, respectively).

REFERENCES

Bleck, R. (2002). An Oceanic General Circulation Model Framed in Hybrid Iopycnic-Cartesian Coordinates. *Ocean Model.* 4, 55–88. doi: 10.1016/S1463-5003(01)00012-9

Bosc, C., and Delcroix, T. (2008). Observed Equatorial Rossby Waves and ENSO-Related Warm Water Volume Changes in the Equatorial Pacific Ocean. *J. Geophys. Res. Ocean* 113, C06003. doi: 10.1029/2007JC004613

Boyd, J. P. (2018). "Kelvin, Yanai, Rossby and Gravity Waves," in *Dynamics of the Equatorial Ocean* (Berlin, Heidelberg: Springer). doi: 10.1007/978-3-662-55476-0_3

Chen, G., Han, W., Li, Y., Wang, D., and McPhaden, M. J. (2015). Seasonal-To-Interannual Time-Scale Dynamics of the Equatorial Undercurrent in the Indian Ocean. *J. Phys. Oceanogr.* 45 (6), 1532–1553. doi: 10.1175/jpo-d-14-0225.1

Chen, G., Han, W., Li, Y., Yao, J., and Wang, D. (2019). Intraseasonal Variability of the Equatorial Undercurrent in the Indian Ocean. *J. Phys. Oceanogr.* 49 (1), 85–101. doi: 10.1175/jpo-d-18-0151.1

Chen, X., Zheng, C., Wu, H., You, X., Li, X., and Wang, H. (2018). Relationship Between a Function of the Northward Pressure Gradient and the Pacific Equatorial Undercurrent. *Acta Oceanol. Sin.* 37 (9), 22–28. doi: 10.1007/s13131-018-1262-9

Coats, S., and Karnauskas, K. B. (2018). A Role for the Equatorial Undercurrent in the Ocean Dynamical Thermostat. *J. Clim.* 31 (16), 6245–6261. doi: 10.1175/jcli-d-17-0513.1

Cromwell, T., Montgomery, R. B., and Stroup, E. D. (1954). Equatorial Undercurrent in Pacific Ocean Revealed by New Methods. *Science* 119 (3097), 648–649. doi: 10.1126/science.119.3097.648

Delcroix, T., Picaut, J., and Eldin, G. (1991). Equatorial Kelvin and Rossby Waves Evidenced in the Pacific Ocean Through Geosat Sea Level and Surface Current Anomalies. *J. Geophys. Res. Ocean* 96 (S01), 3249–3262. doi: 10.1029/90JC01758

Drenkard, E. J., and Karnauskas, K. B. (2014). Strengthening of the Pacific Equatorial Undercurrent in the SODA Reanalysis: Mechanisms, Ocean Dynamics, and Implications. *J. Clim.* 27 (6), 2405–2416. doi: 10.1175/jcli-d-13-00359.1

Errico, R. M. (1997). What Is an Adjoint Model? *Bull. Amer. Meteorol. Soc* 78 (11), 2577–2592. doi: 10.1175/1520-0477(1997)078<2577:wiaam>2.0.co;2

Firing, E., Lukas, R., Sadler, J., and Wyrtki, K. (1983). Equatorial Undercurrent Disappears During 1982-1983 El Nino. *Science* 222 (4628), 1121–1123. doi: 10.1126/science.222.4628.1121

Fukumori, I., Lee, T., Cheng, B., and Menemenlis, D. (2004). The Origin, Pathway, and Destination of Niño-3 Water Estimated by a Simulated Passive Tracer and Its Adjoint. *J. Phys. Oceanogr.* 34 (3), 582–604. doi: 10.1175/2515.1

Gent, P. R., and Mcwilliams, J. C. (1990). Isopycnal Mixing in Ocean Circulation Models. *J. Phys. Oceanogr.* 20 (1), 150–155. doi: 10.1175/1520-0485(1990)020<0150:imiocm>2.0.co;2

Giering, R., and Kaminski, T. (1998). Recipes for Adjoint Code Construction. *ACM Trans. Math. Software* 24 (4), 437–474. doi: 10.1145/293686.293695

Halpern, D., Menemenlis, D., and Wang, X. (2015). Impact of Data Assimilation on ECCO2 Equatorial Undercurrent and North Equatorial Countercurrent in the Pacific Ocean. *J. Atmos. Ocean. Technol.* 32 (1), 131–143. doi: 10.1175/jtech-d-14-00025.1

Heimbach, P., Hill, C., and Giering, R. (2005). An Efficient Exact Adjoint of the Parallel MIT General Circulation Model, Generated *via* Automatic Differentiation. *Futur. Gener. Comp. Syst.* 21 (8), 1356–1371. doi: 10.1016/j.future.2004.11.010

Huang, R., and Jin, F. (2003). The Asymmetric Nature of the Equatorial Undercurrent in the Pacific and Atlantic. *J. Phys. Oceanogr.* 33 (5), 0022–3670. doi: 10.1175/1520-0485(2003)033<1083:tanote>2.0.co;2

Hu, D., Wu, L., Cai, W., Gupta, A. S., Ganachaud, A., Qiu, B., et al. (2015). Pacific Western Boundary Currents and Their Roles in Climate. *Nature* 522 (7556), 299–308. doi: 10.1038/nature14504

Izumo, T. (2005). The Equatorial Undercurrent, Meridional Overturning Circulation, and Their Roles in Mass and Heat Exchanges During El Niño Events in the Tropical Pacific Ocean. *Ocean Dyn.* 55 (2), 110–123. doi: 10.1007/s10236-005-0115-1

Johnson, G. C., McPhaden, M. J., Rowe, G. D., and McTaggart, K. E. (2000). Upper Equatorial Pacific Ocean Current and Salinity Variability During the 1996–1998 El Niño–La Niña Cycle. *J. Geophys. Res. Ocean* 105 (C1), 1037–1053. doi: 10.1029/1999JC900280

Johnson, G. C., Sloyan, B. M., Kessler, W. S., and McTaggart, K. E. (2002). Direct Measurements of Upper Ocean Currents and Water Properties Across the Tropical Pacific During the 1990s. *Prog. Oceanogr.* 52 (1), 31–61. doi: 10.1016/S0079-6611(02)00021-6

Jones, D. C., Forget, G., Sinha, B., Josey, S. A., Boland, E. J. D., Meijers, A. J. S., et al. (2018). Local and Remote Influences on the Heat Content of the Labrador Sea: An Adjoint Sensitivity Study. *J. Geophys. Res. Ocean* 123, 2646– 2667. doi: 10.1002/2018JC013774

Junge, M. M., and Haine, T. W. N.. (2001). Mechanisms of North Atlantic Wintertime Sea Surface Temperature Anomalies. *J. Clim.* 14(24), 4560-4572. doi: 10.1175/1520-0442(2001)014<4560:monaws>2.0.co;2

Kalnay, E., Kanamitsu, M., Kistler, R., Collins, W., Deaven, D., Gandin, L., et al. (1996). The NCEP/NCAR 40-Year Reanalysis Project. *Bull. Amer. Meteor. Soc.* 77 (3), 437–472. doi: 10.1175/1520-0477(1996)077<0437:TNYRP>2.0.CO;2

Kessler, W. S., Rothstein, L. M., and Chen, D. (1998). The Annual Cycle of SST in the Eastern Tropical Pacific, Diagnosed in an Ocean GCM. *J. Clim.* 11 (5), 777–799. doi: 10.1175/1520-0442(1998)011<0777:tacosi>2.0.co;2

Köhl, A., and Stammer, D. (2008). Variability of the Meridional Overturning in the North Atlantic From the 50-Year GECCO State Estimation. *J. Phys. Oceanogr.* 38 (9), 1913–1930. doi: 10.1175/2008jpo3775.1

Köhl, A., Stammer, D., and Cornuelle, B. (2007). Interannual to Decadal Changes in the ECCO Global Synthesis. *J. Phys. Oceanogr.* 37 (2), 313–337. doi: 10.1175/jpo3014.1

Köhl, A., and Vlasenko, A. (2019). Seasonal Prediction of Northern European Winter Air Temperatures From SST Anomalies Based on Sensitivity Estimates. *Geophys. Res. Lett.* 46 (11), 6109–6117. doi: 10.1029/2018GL081800

Large, W. G., McWilliams, J. C., and Doney, S. C. (1994). Oceanic Vertical Mixing: A Review and a Model With a Nonlocal Boundary Layer Parameterization. *Rev. Geophys.* 32 (4), 363–403. doi: 10.1029/94RG01872

Liu, C., Köhl, A., and Stammer, D. (2012). Adjoint-Based Estimation of Eddy-Induced Tracer Mixing Parameters in the Global Ocean. *J. Phys. Oceanogr.* 42 (1186), 0022–3670. doi: 10.1175/jpo-d-11-0162.1

Liu, Z., and Philander, S. G. H. (1995). How Different Wind Stress Patterns Affect the Tropical-Subtropical Circulations of the Upper Ocean. *J. Phys. Oceanogr.* 25 (4), 449–462. doi: 10.1175/1520-0485(1995)025<0449:hdwspa>2.0.co;2

Locarnini, R. A., Mishonov, A. V., Antonov, J. I., Boyer, T. P., Garcia, H. E., Baranova, O. K., et al. (2013). World ocean atlas 2013, Volume 1: Temperature. In S. Levitus and A. Mishonov (Eds.), *NOAA Atlas NESDIS* (Vol. 73, p. 39). doi: 10.7289/V55X26VD

Lyu, Y., Li, Y., Wang, J., Duan, J., Tang, X., Liu, C., et al. (2020). Anomalous Upper-Ocean Circulation of the Western Equatorial Pacific Following El Niño Events. *J. Phys. Oceanogr.* 50 (11), 3353–3373. doi: 10.1175/jpo-d-20-0011.1

Marotzke, J., Giering, R., Zhang, K. Q., Stammer, D., Hill, C., and Lee, T. (1999). Construction of the Adjoint MIT Ocean General Circulation Model and Application to Atlantic Heat Transport Sensitivity. *J. Geophys. Res. Ocean* 104, 29,529. doi: 10.1029/1999jc900236

Marshall, J., Adcroft, A., Hill, C., Perelman, L., and Heisey, C. (1997). A Finite-Volume, Incompressible Navier Stokes Model for Studies of the Ocean on Parallel Computers. *J. Geophys. Res. Ocean* 102 (C3), 5753–5766. doi: 10.1029/96JC02775

Mazloff, M. R., Heimbach, P., and Wunsch, C. (2010). An Eddy-Permitting Southern Ocean State Estimate. *J. Phys. Oceanogr.* 40 (5), 880–899. doi: 10.1175/2009JPO4236.1

McCreary, J. (1976). Eastern Tropical Ocean Response to Changing Wind Systems: With Application to El Niño. *J. Phys. Oceanogr.* 6 (5), 632–645. doi: 10.1175/1520-0485(1976)006<0632:etortc>2.0.co;2

McPhaden, M. J. (1981). Continuously Stratified Models of the Steady-State Equatorial Ocean. *J. Phys. Oceanogr.* 11 (3), 337–354. doi: 10.1175/1520-0485(1981)011<0337:csmots>2.0.co;2

McPhaden, M. J., and Taft, B. A. (1988). Dynamics of Seasonal and Interannual Variability in the Eastern Equatorial Pacific. *J. Phys. Oceanogr.* 18 (11), 1713–1732. doi: 10.1175/1520-0485(1988)018<1713:DOSAIV>2.0.CO;2

Pedlosky, J. (1987). An Inertial Theory of the Equatorial Undercurrent. *J. Phys. Oceanogr.* 17 (11), 1978–1985. doi: 10.1175/1520-0485(1987)017<1978:aitote>2.0.co;2

Pennington, J. T., Mahoney, K. L., Kuwahara, V. S., Kolber, D. D., Calienes, R., and Chavez, F. P. (2006). Primary Production in the Eastern Tropical Pacific: A Review. *Prog. Oceanogr.* 69 (2), 285–317. doi: 10.1016/j.pocean.2006.03.012

Philander, S. G. H., Hurlin, W. J., and Seigel, A. D. (1987). Simulation of the Seasonal Cycle of the Tropical Pacific Ocean. *J. Phys. Oceanogr.* 17 (11), 1986–2002. doi: 10.1175/1520-0485(1987)017<1986:sotsco>2.0.co;2

Qin, X., Sen Gupta, A., and van Sebille, E. (2015). Variability in the Origins and Pathways of Pacific Equatorial Undercurrent Water. *J. Geophys. Res. Ocean* 120 (4), 3113–3128. doi: 10.1002/2014JC010549

Redi, M. H. (1982). Oceanic Isopycnal Mixing by Coordinate Rotation. *J. Phys. Oceanogr.* 12 (10), 1154–1158. doi: 10.1175/1520-0485(1982)012<1154:oimbcr>2.0.co;2

Smith, W. H. F., and Sandwell, D. T. (1997). Global Sea Floor Topography From Satellite Altimetry and Ship Depth Soundings. *Science* 277 (5334), 1956–1962. doi: 10.1126/science.277.5334.1956

Stommel, H. (1959). Wind-Drift Near the Equator. *Deep-Sea Res.* 6, 298–302. doi: 10.1016/0146-6313(59)90088-7

Verdy, A., Mazloff, M. R., Cornuelle, B. D., and Kim, S. Y. (2014). Wind-Driven Sea Level Variability on the California Coast: An Adjoint Sensitivity Analysis. *J. Phys. Oceanogr.* 44 (1), 297–318. doi: 10.1175/jpo-d-13-018.1

Wang, X., Liu, C., Köhl, A., Geng, W., Wang, F., and Stammer, D. (2021). The Adjoint-Based Two Oceans One Sea State Estimate (TOOSSE). *J. Oceanol. Limnol.* 40, 1–21. doi: 10.1007/s00343-021-0439-9

Yu, X., and McPhaden, M. J. (1999). Dynamical Analysis of Seasonal and Interannual Variability in the Equatorial Pacific. *J. Phys. Oceanogr.* 29 (9), 2350–2369. doi: 10.1175/1520-0485(1999)029<2350:daosai>2.0.co;2

Zhang, X., Cornuelle, B., and Roemmich, D. (2011). Adjoint Sensitivity of the Ni?o-3 Surface Temperature to Wind Forcing. *J. Clim.* 24 (16), 4480–4493. doi: 10.1175/2011jcli3917.1

Zweng, M. M., Reagan, J. R., Antonov, J. I., Locarnini, R. A., Mishonov, A. V., Boyer, T. P., et al. (2013). World ocean atlas 2013, volume 2: Salinity. In S. Levitus and A. Mishonov (Eds.), *NOAA Atlas NESDIS* (Vol. 74, p. 40). doi: 10.7289/V5251G4D